Asynchronous Crystal Cell Expansion during Lithiation of K + -Stabilized α-MnO 2

13 AUTHORS, INCLUDING:

Sunand Santhanagopalan
University of Texas at Arlington
11 PUBLICATIONS **194** CITATIONS

SEE PROFILE

Dennis Desheng Meng
Michigan Technological University
20 PUBLICATIONS **312** CITATIONS

SEE PROFILE

R. F. Klie
University of Illinois at Chicago
212 PUBLICATIONS **2,667** CITATIONS

SEE PROFILE

Christopher S Johnson
Argonne National Laboratory
69 PUBLICATIONS **3,640** CITATIONS

SEE PROFILE

Asynchronous Crystal Cell Expansion during Lithiation of K+-Stabilized α-MnO2

Yifei Yuan,[†,‡] Anmin Nie,*[,§] Gregory M. Odegard,[§] Rui Xu,[‡] Dehua Zhou,[‡] Sunand Santhanagopalan,[§,‖] Kun He,[†,⊥] Hasti Asayesh-Ardakani,[§] Dennis Desheng Meng,[§,‖] Robert F. Klie,[∇] Christopher Johnson,[‡] Jun Lu,[‡] and Reza Shahbazian-Yassar*[,§]

[†]Department of Materials Science and Engineering, Michigan Technological University, 1400 Townsend Drive, Houghton, Michigan 49931, United States

[‡]Chemical Science and Engineering Division, Argonne National Laboratory, 9700 South Cass Avenue, Argonne, Illinois 60439, United States

[§]Department of Mechanical Engineering, Michigan Technological University, 1400 Townsend Drive, Houghton, Michigan 49931, United States

[‖]Department of Mechanical and Aerospace Engineering, University of Texas at Arlington, 500 West First Street, Arlington, Texas 76019, United States

[⊥]Department of Materials Science and Engineering, Shandong University, 17923 Jingshi Road, Jinan 250061, China

[∇]Department of Physics, University of Illinois at Chicago, 845 West Taylor Street, Chicago, Illinois 60607, United States

S *Supporting Information*

ABSTRACT: α-MnO2 is a promising material for Li-ion batteries and has unique tunneled structure that facilitates the diffusion of Li+. The overall electrochemical performance of α-MnO2 is determined by the tunneled structure stability during its interaction with Li+, the mechanism of which is, however, poorly understood. In this paper, a novel tetragonal–orthorhombic–tetragonal symmetric transition during lithiation of K+-stabilized α-MnO2 is observed using in situ transmission electron microscopy. Atomic resolution imaging indicated that 1×1 and 2×2 tunnels exist along c ([001]) direction of the nanowire. The morphology of a partially lithiated nanowire observed in the ⟨100⟩ projection is largely dependent on crystallographic orientation ([100] or [010]), indicating the existence of asynchronous expansion of α-MnO2's tetragonal unit cell along a and b lattice directions, which results in a tetragonal–orthorhombic–tetragonal (TOT) symmetric transition upon lithiation. Such a TOT transition is confirmed by diffraction analysis and Mn valence quantification. Density functional theory (DFT) confirms that Wyckoff 8h sites inside 2×2 tunnels are the preferred sites for Li+ occupancy. The sequential Li+ filling at 8h sites leads to asynchronous expansion and symmetry degradation of the host lattice as well as tunnel instability upon lithiation. These findings provide fundamental understanding for appearance of stepwise potential variation during the discharge of Li/α-MnO2 batteries as well as the origin for low practical capacity and fast capacity fading of α-MnO2 as an intercalated electrode.

KEYWORDS: *in-situ TEM, Li-ion batteries, MnO2, nanowires, tunneled structure*
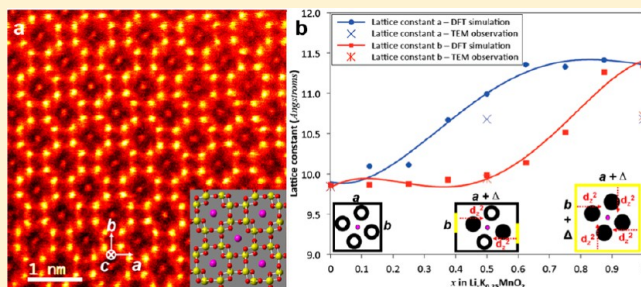
Manganese dioxide (MnO2) is well known as an important functional metal oxide being applied in the fields of biosensor, ion exchange, catalysis, molecular adsorption, and particularly energy storage.[1−4] These various applications originate from the polymorphic property of MnO2, which allows the existence of different structural forms (α-, β-, γ-, and δ-types, etc.).[5−7] These forms differ in the way the structure units ([MnO6] octahedra) are interlinked. As such, they possess interlayers or tunnels with gaps of different sizes in the angstrom range.[8] Figure 1 illustrates crystal structures of tunnel-based MnO2 polymorphs. Among them, hollandite α-MnO2 is body-centered tetragonal with $I4/m$ space group and

has one-dimensional 2×2 (4.6 Å × 4.6 Å) and 1×1 (1.9 Å × 1.9 Å) tunnels intergrowth along c axis,[8] as shown in Figures 1c and d. The 2×2 tunnels are generally stabilized by cations (NH4+, Ba2+, Ag+, K+, etc.) introduced during the synthesis process.[2,9]

Its low cost, natural abundance,[10] and environmental friendliness[11] make α-MnO2 one of the most important materials for electric energy storage in lithium ion battery,
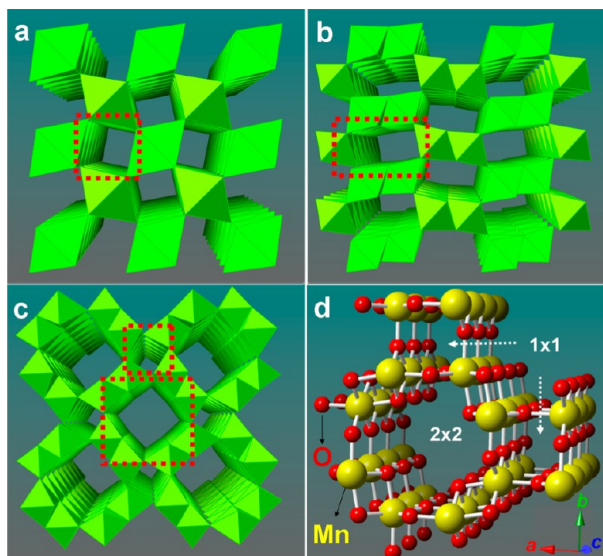
Figure 1. (a−c) Crystal structures of β-MnO$_2$ (1 × 1 tunnel), γ-MnO$_2$ (1 × 2 tunnel), and α-MnO$_2$ (1 × 1 and 2 × 2 tunnels) using [MnO$_6$] octahedra model demonstrating the tunnel structures by red dashed squares. (d) Atomic structure of one 2 × 2 tunnel and two adjacent 1 × 1 tunnels of α-MnO$_2$ growing along [001] (c axis).

supercapacitor, and Li−O$_2$ battery. For this application, the presence of tunnels plays a key role as the reversible capacity is largely determined by tunnel-driven (de)intercalation of Li$^+$.[12−14] α-MnO$_2$ is believed to show topotactic reduction of Mn (Li$^+$ solid solution) during lithiation. Specifically, partially lithiated α-MnO$_2$ was reported to show identical expansion tendency along a and b directions, and thus, the tetragonal symmetry is maintained without any phase transition.[15−17] On the other hand, several groups pointed out that the first galvanostatic discharge curve of Li/α-MnO$_2$ battery was characterized by stepwise potential variation or obvious voltage multiplateaus, indicating existence of phase transition.[18−20] Yet, none of them could provide direct structural evidence for these specific lithiation stages. In addition, it is still unclear what is the origin for the commonly observed low electrode utilization of α-MnO$_2$, where the discharge capacity is less than 60% of the theoretical value.[20]

These uncertainties result mainly from two practical limitations: First, it is difficult to precisely characterize angstrom-sized tunnels in MnO$_2$ due to resolution limitations of the most characterization techniques. Second, under electrochemical cycling, it is difficult to acquire structural and compositional information with any conventional ex-situ electrochemistry methods. In-situ transmission electron microscopy (TEM) nanoscale electrochemistry studies using an
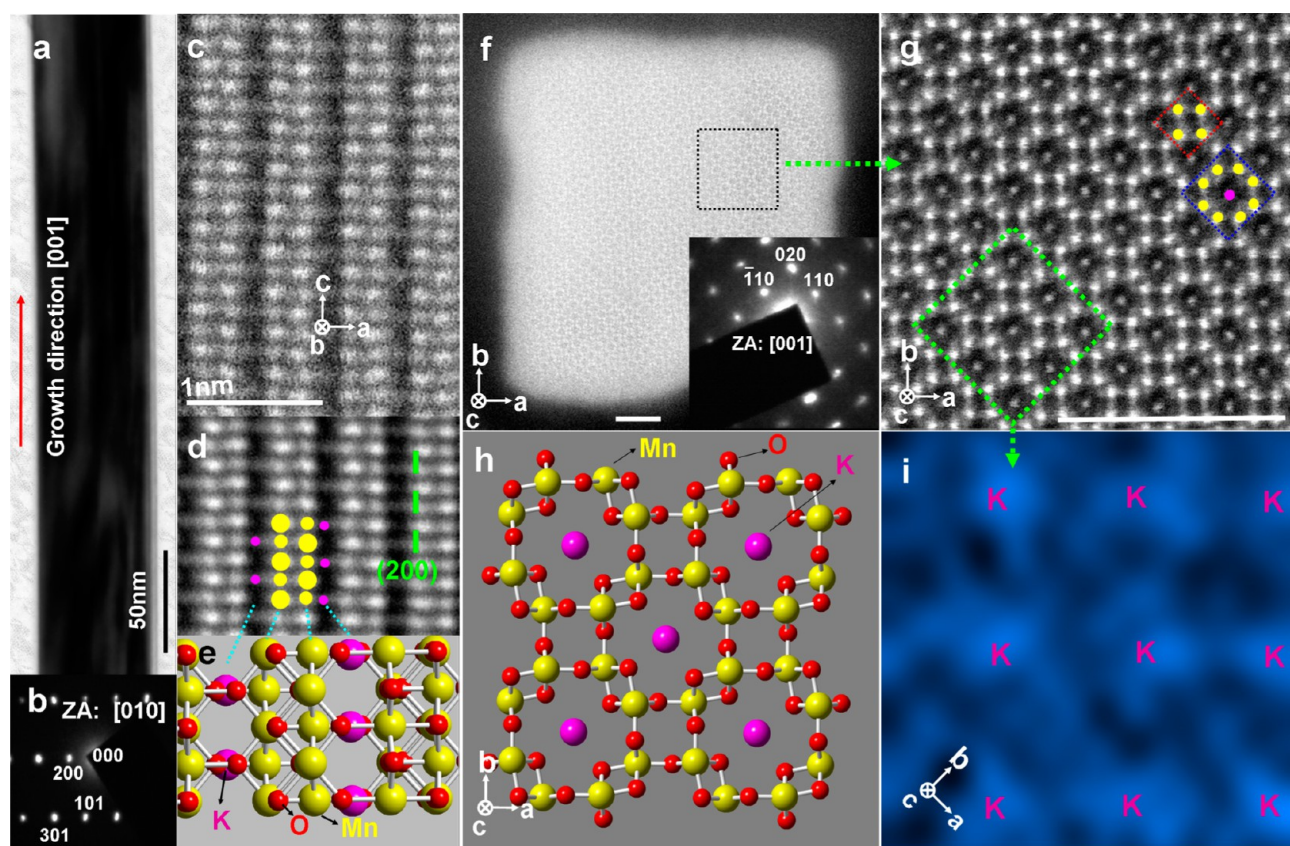

Figure 2. (a,b) TEM image of a single α-MnO$_2$ nanowire and its SAED along ⟨010⟩. (c) HAADF image of the same α-MnO$_2$ nanowire along ⟨010⟩. (d,e) IFFT of the original HAADF shown in (c) and the atomic model structure along ⟨010⟩ direction, respectively. Yellow spots indicate Mn atoms, whereas pink represents K and red indicates O atoms. (f) HAADF image of an α-MnO$_2$ nanowire cross section and the corresponding SAED along [001] direction. (g) Atomic resolution HAADF image of an area in f (black dotted box) showing Mn atomic column (yellow), K column (pink), 1 × 1 (red dotted square) and 2 × 2 (blue dotted square) tunnels. Scale bars in (f) and (g) are both 3 nm. (h) Simulated image of K$^+$-occupied α-MnO$_2$ viewed along [001] direction. (i) EDS mapping of the green dotted box in (g) confirms the center atoms to be K (this figure is rotated 45° compared to (g) for viewer's convenience).
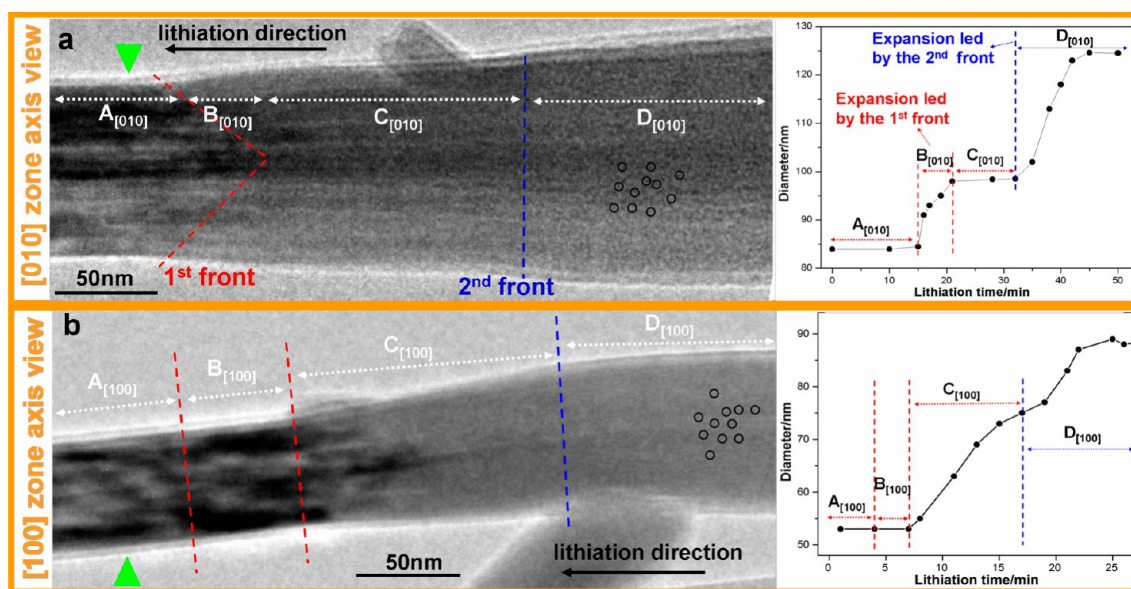
Figure 3. (a) [010] TEM projection of a partially lithiated α-MnO₂ nanowire showing two lithiation reaction fronts. The red dashed line corresponds to the first reaction front and the blue dashed line relates to the second reaction front. Four zones with different characteristics are defined: Zone A[010] for unlithiated section of the nanowire, Zone B[010] for the expanded region associate with the first reaction front, Zone C[010] for the section with a constant diameter surrounded between two reaction fronts, and Zone D[010] for the fully expended region associated with the second reaction front and featured by numerous nanodomains (black circles). The right graph shows diameter evolution during lithiation. (b) [100] projection of the partially lithiated α-MnO₂ nanowire showing a gradually expanding zone. Similarly, four zones are defined: Zone A[100] for pristine nanowire, Zone B[100] for stressed (dark contrast) section without diameter expansion, Zone C[100] for gradually expanding section, and Zone D[100] for the final lithiated state featured by numerous nanodomains (black circles). The right graph shows diameter evolution during lithiation. The green triangles in panels a and b indicate the fixed positions on two nanowires for diameter measurement.

"open-cell" concept has recently been developed[21] and proved later by many experiments to be powerful in real-time study of electrode materials such as graphene,[22] Si,[23−25] Ge,[26] CuO,[27] ZnO,[28] TiO₂,[29] SnO₂,[30] FeF₂,[31] LiFePO₄,[32] and different nanocomposites[33−35] under electrochemical cycling.

In this paper, in situ scanning TEM (STEM) was used for the study of lithiation behavior in single crystalline α-MnO₂ nanowire. Local morphological changes including lattice expansion and Mn valence evolution of the nanowire during dynamic lithiation process are revealed. Our findings show that α-MnO₂ nanowire exhibits two types of tunnels: 1 × 1 and K⁺-stabilized 2 × 2 tunnels. Lithiation of α-MnO₂ nanowires is characterized by asynchronous expansion behavior of lattice parameters a and b, resulting in a tetragonal−orthorhombic−tetragonal (TOT) symmetrical transition of lithiated α-MnO₂. This is contradicting to the widely accepted understanding that a and b lattice parameters expand synchronously when tetragonal α-MnO₂ is discharged. DFT calculation reveals that the asynchronous lattice expansion originates from Li⁺ preferably occupying Wyckoff 8h sites inside 2 × 2 tunnels in a specific sequence. The symmetry transition of α-MnO₂ electrode during lithiation is expected to explain the appearance of stepwise potential variations during discharge and the commonly observed low electrode utilization in Li/MnO₂ batteries.[10,36,37]

Figure 2 shows the atomic structure of an α-MnO₂ nanowire prepared via hydrothermal method.[38] Figure 2a and b indicate that the nanowire is single crystalline α-MnO₂ phase with growth direction (c axis) along [001]. HAADF image of the nanowire viewed along ⟨010⟩ is given in Figure 2c with the corresponding inverse fast Fourier transform (IFFT) image and simulated crystal structure along ⟨010⟩ direction given in Figure 2d and e, respectively. The Mn atomic columns, marked

by yellow dots in IFFT, can be easily identified. The appearance of O atoms in every two Mn columns contributes to the alternative changes in the brightness of Mn columns as marked by the yellow dots in two different sizes (Figure 2d). Close examination of Figure 2c and d indicates that there are extra atomic columns lining up between two Mn columns, as marked by the pink dots. Considering the hydrothermal synthesis where potassium (K⁺) was present (see Supporting Information), these extra columns are indicative of K atoms acting as stabilizers inside 2 × 2 tunnels of α-MnO₂. This was subsequently confirmed by energy dispersive spectroscopy (EDS) as discussed in the following.

The HAADF image in Figure 2f shows the cross section of an α-MnO₂ nanowire viewed along [001] zone axis (inset). The sample preparation method is provided in the Supporting Information. The magnified HAADF image in Figure 2g clearly shows that the atomic structure consists of two types of tunnels: the small 1 × 1 tunnels and the large 2 × 2 tunnels as indicated by the red and blue dashed squares, respectively. This definition is based on the number of [MnO₆] octahedra in each side.[39] The 1 × 1 tunnels are expected to have limited contribution to the discharge capacity, whereas 2 × 2 tunnels determine the overall discharge capacity in cathodic application of α-MnO₂ nanowires.[40]

The bright spots surrounding each tunnel refer to Mn ([MnO₆]) atomic columns (yellow dots), whereas the spots in the center of each 2 × 2 tunnel belongs to K ions (pink dots), as confirmed by EDS mapping of K signal in Figure 2i. To the authors' knowledge, this [001] zone axis image is the first atomistic observation of the tunneled structure in α-MnO₂ capturing the position of tunnel stabilizers. Considering Figure 2d and g, the Wyckoff position of K⁺ in α-MnO₂ is determined to be 2a site (0, 0, 0), which is in excellent agreement with the
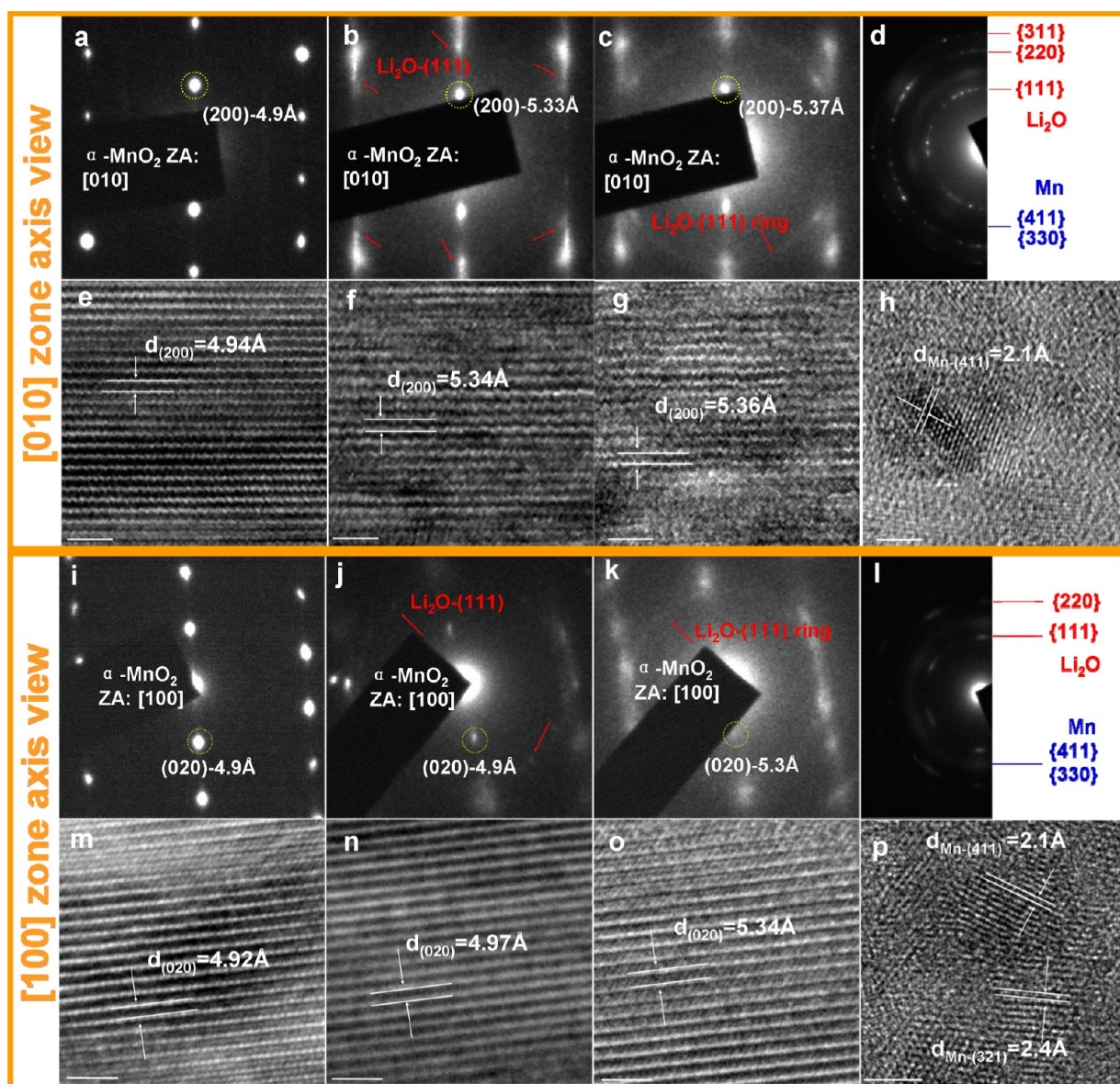
Figure 4. (a−d) Corresponding SAED patterns from the four zones shown in Figure 3a. SAED pattern shown in (a) is for Zone A$_{[010]}$, (b) from the right end of Zone B$_{[010]}$, (c) from the right end of Zone C$_{[010]}$ and (d) for Zone D$_{[010]}$. (e−h) Corresponding HRTEM images from the same four areas as defined for SAED in (a−d). (i−l) Corresponding SAED patterns from the four lithiation zones shown in Figure 3b where (i) is for Zone A$_{[100]}$, (j) is from the right end of Zone B$_{[100]}$, (k) is from the right end of Zone C$_{[100]}$, and (l) is for Zone D$_{[100]}$. (m−p) Corresponding HRTEM images from the same four areas as defined for SAED in (i−l). The scale bar is 2 nm for all HRTEM images.

theoretical K$^+$ position.[41] The composition of the nanowire is thus determined to be K$_{0.25}$MnO$_2$.

The in situ setup and time sequence TEM images of an α-MnO$_2$ nanowire during lithiation along [010] zone axis are shown in Figure S1 and Movie S1 (Supporting Information). They show that the lithiation process is associated with two distinct expansion fronts. The first expansion front proceeds quickly (42 nm/min on average) along the nanowire and results in fast radial expansion. Subsequently, the second expansion happens with slower propagation speed (28 nm/min) than the first reaction front, indicating lithiation retardation probably due to the electrochemical-induced stresses. The section squeezed by these two reaction fronts maintains a constant diameter. For another α-MnO$_2$ nanowire viewed along [100] zone axis, however, the lithiation process is sharply different as shown in Supporting Information Figure S2.

In this nanowire, one cannot detect the two reaction front phenomena during lithiation, and instead, a gradual increase in diameter was observed. This is intriguing knowing that the [010] and [100] zone axes of α-MnO$_2$ should essentially exhibit similar lithiation behavior due to the tetragonal crystal symmetry. It is unlikely that such a deviation is due to any experimental error as this observation was repeatable for nanowires under [010] (Supporting Information Figures S3, S4a) and [100] (Supporting Information Figure S4b, Movie S2) zone axes. It is worth mentioning that some pristine nanowires show "bundling" phenomenon (Figures 3a and 5a and Supporting Information S3 and S4b), which should be caused by lateral oriented attachment (OA) growth mechanism that is widely accepted for solution-grown α-MnO$_2$ nanowires.[39,42,43] This mechanism is also confirmed in Supporting Information Figure S5 showing that one secondary nanowire

branches at its end while still maintains single crystalline property. Considering the fact that the OA mechanism still results in single crystals and that the two-step expansion (or single expansion) phenomenon appears in both bundled and nonbundled nanowires (see Supporting Information Figures S1−4) with varying diameters, the size and morphology factors can be excluded.

Figure 3 shows the morphological analysis for the two nanowires viewed along [010] and [100] zone axes. Figure 3a shows the [010] projection of the partially lithiated nanowire where the two-reaction fronts feature is captured. The first reaction front (red dashed line) shows a conical shape visualized by contrast change indicating the existence of surface lithiation.[44] Because the conical angle (about 90°) here is much larger than the previously reported angle (15°−20°)[44] for other materials, longitudinal lithiation is believed to play a key role in the formation of the first reaction front. The second reaction front (blue dashed line) appears to be relatively flat and results in formation of numerous small nanoparticles (marked as black circles) embedded in the matrix. The section between the two reaction fronts has a constant diameter with uniform image contrast implying good structural stability upon lithiation in this area. As such, four zones $A_{[010]}$, $B_{[010]}$, $C_{[010]}$, and $D_{[010]}$ with distinct features are defined in Figure 3a. The quantitative description of changes in the diameter of this nanowire is represented in this figure.

Figure 3b shows the [100] projection of the partially lithiated α-MnO$_2$ nanowire without observation of any two-reaction fronts feature. Instead, a gradually expanding Zone $C_{[100]}$ was observed as seen in the graph in Figure 3b. It is notable that although the two-reaction front feature is not detectable in this case, a highly stressed Zone $B_{[100]}$ appears just ahead of the gradually expanding Zone $C_{[100]}$. Zone $B_{[100]}$ is characterized by the obvious dark contrast, indicating possible existence of lithiation-induced strain in this area. Interestingly, Zone $B_{[100]}$ shows no sign of diameter change.

To better understand the underlying mechanisms responsible for the morphological evaluation of the nanowires viewed at [100] and [010] zone axes during lithiation, phase analysis is carried out. Figure 4a−d show SAED patterns for the four different zones ($A_{[010]}$−$D_{[010]}$) designated in Figure 3a for a partially lithiated nanowire viewed along [010] zone axis. In Zone $A_{[010]}$, the nanowire is still in pristine state (no lithiation). The (200) plane that is parallel to the growth direction [001] has a characteristic spacing of 4.9 Å, which equals to $a/2$ of α-MnO$_2$ unit cell and thus is used as a signature of α-MnO$_2$ tunneled structure. For Zone $B_{[010]}$, the diffraction pattern still belongs to α-MnO$_2$ phase but it is blurred and stretched along [100] direction, indicating the existence of structural distortion due to lattice deflection induced by Li$^+$ intercalation. This can be attributed to Jahn−Teller distortion of [MnO$_6$] units when Mn is partially reduced from smaller Mn^{4+} ions to larger Mn^{3+} ions due to the insertion of Li$^+$.[45] From Zone $A_{[010]}$ to Zone $B_{[010]}$, the (200) spacing increases from 4.9 to 5.3 Å. No distortion is observed along the longitudinal direction [001] further conforming the anisotropic expansion behavior of α-MnO$_2$ as reported by others.[15,46] It is surprising to observe in Figure 4c that the tunneled structure inside Zone $C_{[010]}$ is well maintained with (200) lattice showing no obvious expansion throughout this zone, which is apparently squeezed by two swelling reaction fronts. The microscopically constant (200) spacing should account for the macroscopically observed constant diameter through Zone $C_{[010]}$ in Figure 3a. Figure

4d shows a completely different diffraction pattern for Zone $D_{[010]}$, where the bright and sharp rings are indexed to be polycrystalline Li$_2$O indicating the formation of Li$_2$O following the second lithiation front. The diffused ring(s) relates to the formation of nanoparticles of Mn as shown in Zone $D_{[010]}$ by black circles in Figure 3a. The average diameter of Mn nanoparticles was measured to be 3 nm. HRTEM images in Figures 4e−h for the four zones clearly demonstrate the evolution of α-MnO$_2$ (200) lattice and agree well with corresponding SAED patterns.

Figure 4i−l show SAED patterns for the four lithiation zones marked as $A_{[100]}$−$D_{[100]}$ in Figure 3b. Figure 4i confirms the pristine nanowire to be single crystalline α-MnO$_2$ viewed along [100] zone axis with its (020) spacing of 4.9 Å. The α-MnO$_2$ diffraction pattern in Figure 4j is blurred, indicating lattice distortion possibly due to initial lithiation in Zone $B_{[100]}$. Overall, however, the (020) spacing is still maintained at 4.9 Å without obvious expansion. As evident from the diffraction pattern, small amount of Li$_2$O forms during this stage confirming the existence of initial lithiation. Figure 4k shows that α-MnO$_2$ pattern from Zone $C_{[100]}$ is further blurred but still maintains the tunneled structure as the (020) lattice is still clear and gradually expands from 4.9 to 5.3 Å. Figure 4l shows that the host in Zone $D_{[100]}$ is thoroughly reduced to Mn and Li$_2$O via conversion reaction. Figures 4m−p show HRTEM images of (020) lattice for the four zones and they match the corresponding SAED patterns very well.

The d spacing of 2.1 and 2.4 Å in Figure 4h and p belongs to the $(411)_{Mn}$ and $(321)_{Mn}$ planes, respectively. This confirms the formation of Mn nanoparticles in Zone $D_{[010]}$ and Zone $D_{[100]}$. See also Supporting Information Figure S6 for more evidence. As such, one can conclude that under both [010] and [100] projections, Zone D is the fully lithiated stage featured by conversion reaction usually found in deep discharged transitional metal oxides. In this paper, however, we will not focus on this conversion reaction as it has been discussed extensively by others.[31,47,48]

For nanowires viewed along [100] and [010] zone axes, we focus on Zone $B_{[010]}$ and Zone $B_{[100]}$, Zone $C_{[010]}$ and Zone $C_{[100]}$, where the nanowires are partially lithiated and show interesting morphologies. Considering the facts that {020} spacing reflects the dimension of lattice parameters a and b and that [010] TEM projection is sensitive to the evolution of lattice a but insensitive to that of b (vise versa for [100] projection), we hypothesize that this morphological difference originates from asynchronous expansion of α-MnO$_2$ unit cell along [100] (a direction) and [010] (b direction). Specifically, in the initial Li$^+$ intercalation (zones $B_{[010]}$ and $B_{[100]}$), lattice parameter a is expected to expand with b keeping constant; in the following Li$^+$ intercalation stage (zones $C_{[010]}$ and $C_{[100]}$), it is likely that a remains constant, whereas b expands gradually to catch up with a. During this process, the a/b ratio reaches a maximum value around 1.1 at the end of zones $B_{[010]}$ and $B_{[100]}$ and then returns to 1 at the end of zones $C_{[010]}$ and $C_{[100]}$, resulting in a tetragonal−orthorhombic−tetragonal (TOT) symmetry transition.

It will be discussed below that the proposed asynchronous expansion is associated with sequential filling of tunnels in α-MnO$_2$ with lithium ions. As such, electron energy loss spectroscopy (EELS) was applied to quantify the lithiation degree in zones B and C under both [010] and [100] zone axes by analyzing the Mn valence evolution. Because the chemical signal is less dependent on crystallographic orientation, it is
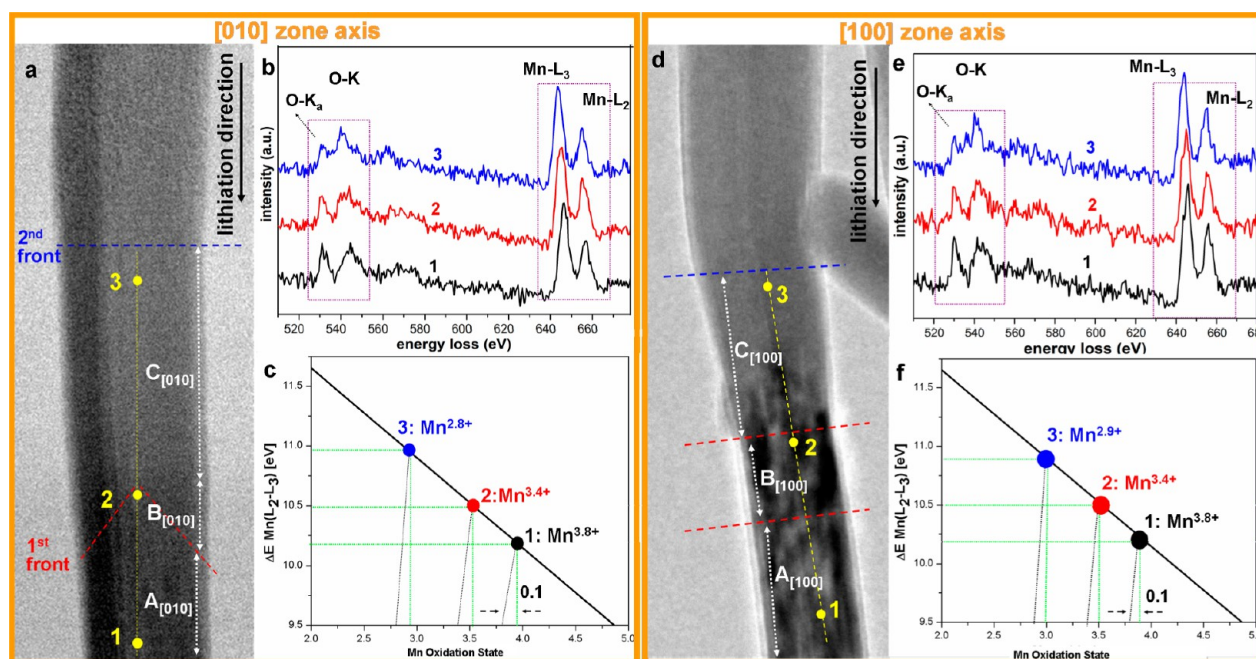
Figure 5. (a,d) [010] and [100] HAADF/TEM images of partially lithiated α-MnO$_2$ nanowires. The EELS data are extracted from three locations on the nanowire, that is, 1 for Zone A$_{[010]}$ and Zone A$_{[100]}$, 2 around the end of Zone B$_{[010]}$ and Zone B$_{[100]}$, 3 around the end of Zone C$_{[010]}$ and Zone C$_{[100]}$. (b,e) The EELS spectra constructed from locations 1, 2, and 3 where the zero loss peak was calibrated as energy reference point. The purple-colored frames indicate O–K edge and Mn–L$_3$/L$_2$ edges. (c,f) Mn valence identification based on reference data using ΔE Mn(L$_2$–L$_3$) fingerprint; the black, red, and blue dots correspond to locations 1, 2, and 3, respectively. Location 1 with known Mn$^{3.8+}$ valence is used to slightly offset the horizontal coordinate value for more precise valence identification of locations 2 and 3.

expected that Mn valence evolution under [010] and [100] projections should show similarity in zones B and C.

To study the oxidation state evolution of Mn during lithiation, EELS line scans were performed on partially lithiated α-MnO$_2$ nanowires viewed along [010] and [100] zone axes. Figure 5a–c depict the analysis for the partially lithiated nanowire under [010] projection, whereas Figure 5d–f represent the nanowire under [100] projection. The EELS data were analyzed from three key locations 1, 2, and 3 indicated by yellow dots on both nanowires to conduct Mn valence analysis. Figure 5b and e show the constructed whole spectra where the prepeak (K$_\alpha$) of oxygen K edge and Mn L$_3$/L$_2$ white lines are indicated. The physical origins of these peaks and observed Mn peak shift are explained in the Supporting Information.

The EELS data for MnO$_2$ have several fingerprints that can be used to quantify Mn valence. The commonly used methods to analyze the valence change include the absolute energy shift of Mn white lines,[49] white-line intensity ratio L$_3$/L$_2$,[50,51] oxygen K prepeak splitting,[52] branching energy difference ΔE(L$_2$–L$_3$)[53] and ΔE(L$_3$–O K$_\alpha$).[54] In our study, ΔE(L$_2$–L$_3$)[53] and ΔE(L$_3$–O K$_\alpha$)[54] are independently used as the fingerprints to analyze Mn valence in different lithiation stages. Considering that K$^+$ presence could slightly alter the Fermi level of α-MnO$_2$, the known valence state of Mn$^{3.8+}$ (unlithiated composition is K$_{0.25}$MnO$_2$, which is rounded to be K$_{0.2}$MnO$_2$ for easier discussion) in location 1 is used as an offset reference to the Mn valence study of locations 2 and 3. Because all the data points are obtained from the same line scan across the same nanowire, these two ΔE methods are less likely to be affected by any instrumental variation.

To better determine the EELS peak positions, the fine structure of each peak is demonstrated in Supporting

Information Figure S7a, b, d and e. Figure 5c and f show the fitted linear curves for ΔE (L$_2$–L$_3$) vs Mn valence from a reference.[53] The symbolic points for locations 1, 2, and 3 are placed accordingly in the graph based on their specific ΔE values obtained from fine analysis in Supporting Information Figures S7b and e. During this process, 0.1 offset value (for the Mn valence state) is calibrated and applied for valence quantification of locations 2 and 3. As such, the valence is determined to be Mn$^{3.4+}$ and Mn$^{2.8+}$ for locations 2 and 3 on [010] projected nanowire, and Mn$^{3.4+}$ and Mn$^{2.9+}$ for locations 2 and 3 on [100] projected nanowire. The alternative quantification method using ΔE(L$_3$–O K$_\alpha$) fingerprint is demonstrated in Supporting Information Figures S7c and f. The Mn valence is determined to be Mn$^{3.5+}$ and Mn$^{3.0+}$ for locations 2 and 3 on [010] projected nanowire, and Mn$^{3.5+}$ and Mn$^{3.0+}$ for locations 2 and 3 on [100] projected nanowire. It is evident that these two independent methods give similar Mn valence evolution in partially lithiated nanowires. For each method, Mn valence evolution from Zone B$_{[010]}$ to Zone C$_{[010]}$ and from Zone B$_{[100]}$ to Zone C$_{[100]}$ is also similar, confirming the proposed asynchronous expansion. By averaging these two methods, experimental Mn valence evolution is determined as following: Mn$^{(3.8+)}$ is reduced to Mn$^{(3.4+)}$ in Zone B; Mn$^{(3.4+)}$ is further reduced to Mn$^{(2.9+)}$ in Zone C; Mn$^{(2.9+)}$ is thoroughly reduced to Mn$^{(0)}$ in the following conversion reaction.

It is known that Jahn–Teller distortion[55] occurs locally around certain [MnO$_6$] units that are close to the insertion sites for lithium.[45] According to our density functional theory (DFT) simulation in Figure 6, there are different sites inside the 2 × 2 tunnels of K$^+$-stabilized α-MnO$_2$ that can accommodate Li$^+$. Interestingly, the center position (2b or 4e) in the tunnel is calculated to be unfavorable for initial lithium insertion, and instead, 8h sites near the tunnel walls
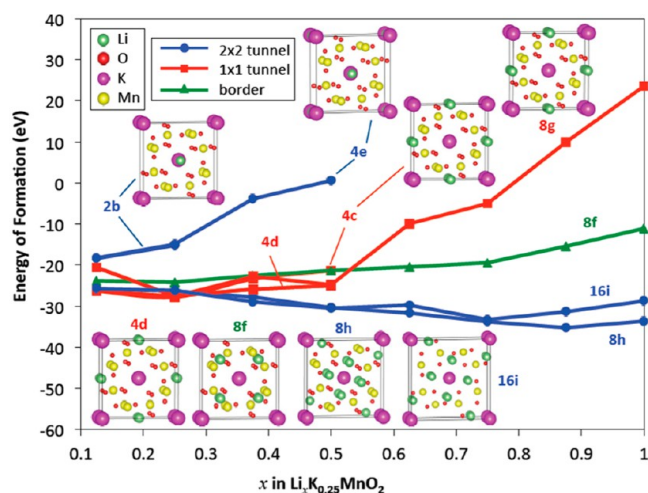
Figure 6. Demonstration of possible Li⁺ insertion sites in α-MnO₂ as well as site occupancy energy calculation for possible Li⁺ insertion sites. It can be seen that 4c, 4d, and 8f sites are also initially preferred for Li⁺ insertion, but their insertion energy increases very fast upon further lithiation. Thus, the capacity contribution from 1 × 1 tunnels can be neglected here. The 8h sites provide the lowest formation energy for Li⁺ insertion up to Li₁K₀.₂₅MnO₂.

provide the lowest binding energy for lithium accommodation up to Li₁MnO₂. The Li⁺ occupancy at 8h sites of each 2 × 2 tunnel is not random but is predicted to exhibit a regular sequence. Figure 7a shows simulated Li⁺ occupancy at 8h sites based on two adjacent 2 × 2 tunnels (there are two tunnels in the periodic unit cell) with K⁺ placed at 2a sites.

It can be seen that when the first lithium occupies the 8h site, the second Li⁺ preferably fills the same site in the adjacent 2 × 2 tunnel (equivalent to K₀.₂₅Li₀.₂₅MnO₂). The third and fourth Li⁺ fill the 8h sites that are the most remote from the first and second Li⁺ in each 2 × 2 tunnel (equaling K₀.₂₅Li₀.₅MnO₂). This behavior is due to their mutual repulsive force, resulting in a low energy configuration. The result is a cooperative Jahn−Teller expansion of the two opposite octahedral [Mn^(3+)O₆] that strengthens each other to achieve unit cell expansion along [100] direction during lithiation Stage 1. Subsequently, inserted Li⁺ ions occupy the remaining 8h sites during lithiation Stage 2. This process is accompanied by another Jahn−Teller expansion

of the unit cell solely along [010] direction. The result of this sequential 8h site filling is asynchronous expansion across a−b plane, where the lattice parameter a first increases in Stage 1, whereas it remains constant in Stage 2. On the other hand, the lattice parameter b remains unchanged in Stage 1 and then increases in Stage 2. The simulated Li⁺ occupancy sequence at 8h sites along [001] direction was also calculated based on a two-layer tunnel model with two Li⁺ inserted. The result is shown in Supporting Information Figure S8 demonstrating five possible scenarios of Li⁺ insertion at 8h sites. It can be seen that when c-axis lithiation is considered, the second Li⁺ prefers to occupy either two remote 8h sites in one 2 × 2 tunnel (Scenario 5) or two 8h sites in two 2 × 2 tunnels aligning parallel to c axis (Scenario 1). Both of these two scenarios, with successive lithiation occurring, can result in a strengthened Jahn−Teller distortion along one specific direction (a-[100]), whereas scenarios 2 (strengthened distortion), 3, and 4 (counterbalanced distortion) are less likely to appear thermodynamically.

Figure 7b illustrates the theoretical DFT calculation of the evolution of lattice parameters a and b as well as the in situ TEM experimental data based on Figures 4 and 5. It can be seen that the trend in differential expansion of lattice parameters a and b is in agreement with TEM observation. However, it can also be seen that the magnitude in the predicted lattice parameters is larger for x > 0.25. This discrepancy in the magnitude is most likely caused by two reasons: first, DFT assumes tunnel stabilizer K⁺ to be fixed at Wyckoff 2a site upon Li⁺ insertion at 8h sites nearby, whereas partial removal of K atoms in the lithiated nanowire was experimentally observed (Supporting Information Figure S9); the second reason is the difficulty with DFT functionals accurately and simultaneously predicting a wide range of physical properties of materials containing transition metal elements and the tendency of PBE functionals to overestimate lattice constants with transition metals.[56] It is speculated that the interconnected 2 × 2 tunnels affect Li⁺ occupancy sequence in each other through a chain interaction. Such an interaction would result in a macroscopically uniform 8h site occupancy configuration. Thus, the nanowire macroscopically experiences asynchronous expansion first along [100] in Zone B and then along [010] direction in Zone C. Figure 8 summarizes the
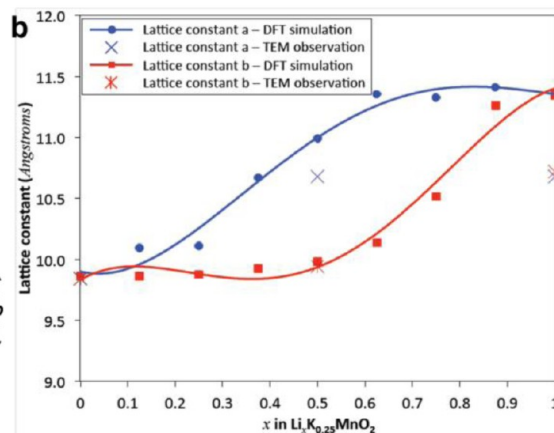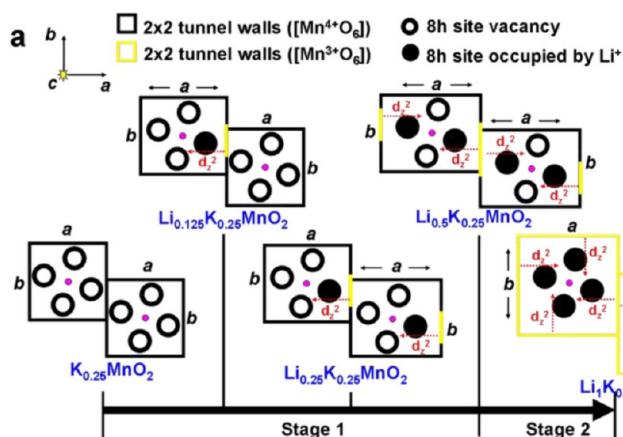

Figure 7. (a) Schematic of the occupancy of 8h sites in the ground state structures of α-K₀.₂₅LiₓMnO₂ (pink dots, K⁺ stabilizers at 2a sites; open circle, unoccupied 8h; solid circle, occupied 8h); d_{z^2} is the orbital that distorts upon Mn reduction by Li⁺ insertion. (b) Predicted behavior of lattice parameters a and b upon lithiation as well as their experimentally observed behavior during lithiation obtained from Figures 4 and 5.
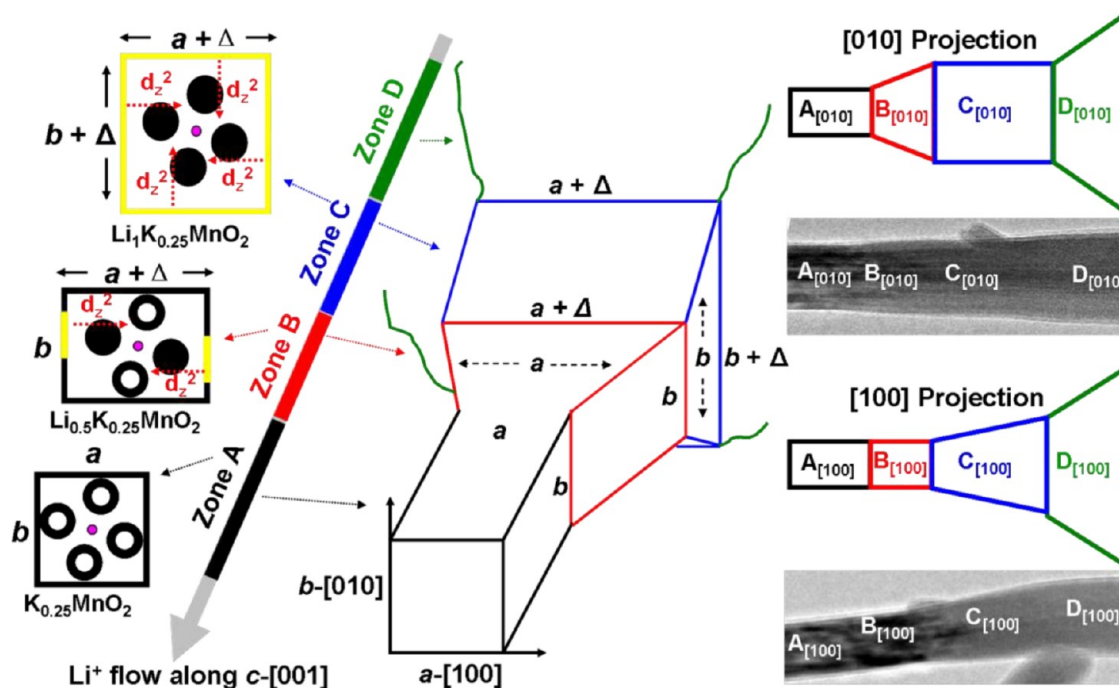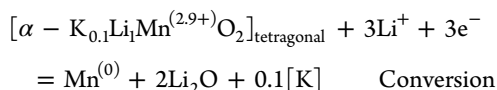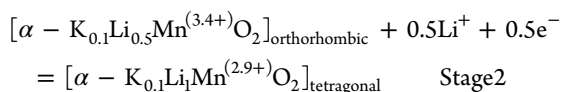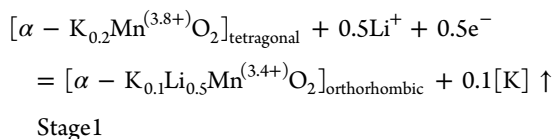
Figure 8. Left: Simulated Li$^+$ occupancy sequence at 8h sites in one 2 × 2 tunnel. Middle: 3D model showing the asynchronous expansion of single α-K$_{0.25}$MnO$_2$ nanowire upon lithiation. Right: Predicted and observed morphology of one partially lithiated α-K$_{0.25}$MnO$_2$ nanowire under [010] and [100] projections.

whole process starting from unit cell simulation to experimental TEM observation.

As such, the full discharge process in single α-K$_{0.2}$Mn$^{(3.8+)}$O$_2$ nanowire can be written as

$$[\alpha - \text{K}_{0.2}\text{Mn}^{(3.8+)}\text{O}_2]_{\text{tetragonal}} + 0.5\text{Li}^+ + 0.5\text{e}^-$$

$$= [\alpha - \text{K}_{0.1}\text{Li}_{0.5}\text{Mn}^{(3.4+)}\text{O}_2]_{\text{orthorhombic}} + 0.1[\text{K}] \uparrow$$

Stage1

$$[\alpha - \text{K}_{0.1}\text{Li}_{0.5}\text{Mn}^{(3.4+)}\text{O}_2]_{\text{orthorhombic}} + 0.5\text{Li}^+ + 0.5\text{e}^-$$

$$= [\alpha - \text{K}_{0.1}\text{Li}_1\text{Mn}^{(2.9+)}\text{O}_2]_{\text{tetragonal}} \qquad \text{Stage2}$$

$$[\alpha - \text{K}_{0.1}\text{Li}_1\text{Mn}^{(2.9+)}\text{O}_2]_{\text{tetragonal}} + 3\text{Li}^+ + 3\text{e}^-$$

$$= \text{Mn}^{(0)} + 2\text{Li}_2\text{O} + 0.1[\text{K}] \qquad \text{Conversion}$$

It is difficult to clearly distinguish and quantify the sole effect of K$^+$ in this process due to its low concentration, so half of the K atoms are roughly supposed to be removed upon initial lithiation. The release of K stabilizers during tunnel degradation was possibly due to the weakening of tunnel restriction and their volatilization in vacuum environment.[57]

Such a TOT symmetry transition involves Li$^+$ accommodation in 8h sites with different insertion energy and can thus potentially account for the appearance of double cathodic peaks in the first cycle cyclic voltammetry curve of Li/α-MnO$_2$ batteries (Supporting Information Figure S10). The reoccurrence of double peaks in the anodic scanning indicates that such a transition is reversible. To further demonstrate the symmetry transition, the phase evolution during the first cycle of Li/α-MnO$_2$ battery is investigated using in situ synchrotron XRD in Supporting Information Figure S11. It shows that among all characteristic peaks of α-MnO$_2$, {200} and {600} show relatively apparent peak broadening upon lithiation. This

is reasonable considering that they are directly related to the dimension of a (b). Besides the peak broadening, a weak shoulder peak ($\approx$5.2 Å) splits away from {200} main peak ($\approx$4.9 Å) during lithiation and stays until the cycle ends. The expanded 5.2 Å spacing is close to TEM observed value ($\approx$5.3 Å) for expanded {200}. This peak splitting could thus be ascribed to the asynchronous expansion between a and b, indicating the existence of TOT transition in the working Li/α-MnO$_2$ coin cell. Similar phenomenon was also reported in a recently published work using in situ synchrotron XRD technique,[58] where "excessive line broadening" and "diffuse splitting of the peaks" were observed for a working Li/α-MnO$_2$ battery and an unknown phase transition was proposed. In this sense, the current work here reasonably explains the underlying phase transition. There are, however, many other factors that could potentially affect the peaks behavior considering the complicated electrochemical environment inside a large-scale coin cell rather than in the single nanowire-based open cell design. The related discussion is given in Supporting Information.

In summary, tetragonal α-MnO$_2$ is featured by 1 × 1 and 2 × 2 tunnels. The 2 × 2 tunnels are supported by K$^+$ and 1 × 1 tunnel are unfilled. DFT calculations show that 1 × 1 tunnels have limited contribution to the discharge capacity of Li/α-MnO$_2$ batteries. On the other hand, the 8h sites inside 2 × 2 tunnels are the most favorable sites for lithiation and, thus, determine the overall discharge capacity for the application of α-MnO$_2$ as a cathode material. In-situ TEM study reveals asynchronous expansion of tetragonal unit cell in α-MnO$_2$ along a and b lattice directions upon lithiation. Specifically, in the first intercalation Stage 1, lattice parameter a expands while b keeps constant; in the following intercalation Stage 2, a remains constant while b expands gradually to catch up with a. Such an asynchronous expansion behavior is well understood by our DFT calculation showing an energy-guided Li$^+$

occupancy sequence at 8h sites inside each 2×2 tunnel. This asynchronous behavior leads to a TOT symmetry transition in α-MnO_2 upon lithiation, which is believed to account for the appearance of multilithiation stages when Li/α-MnO_2 battery is discharged. The degradation of initial tetragonal symmetry and resulted structural instability in α-MnO_2 host during lithiation are expected to explain the commonly observed low electrode utilization of α-MnO_2 in Li/α-MnO_2 batteries.

Our research provides fundamental understanding of lithiation property of α-MnO_2 and explores origins for its specific electrochemical behaviors, casting light on possible compositional modification and structural design to improve its energy storage performance in supercapacitor as well as Li/α-MnO_2 and Li$-O_2$ batteries. Such an asynchronous expansion behavior is expected to exist not only in Li^+ storage but also for Na^+ storage, as Na^+ and Li^+ both carry one charge and their ionic radii are both much smaller than the tunnel size in α-MnO_2.

■ ASSOCIATED CONTENT

ⓢ **Supporting Information**

Additional figures/movies and experimental and simulation details are included. This material is available free of charge via the Internet at http://pubs.acs.org.

■ AUTHOR INFORMATION

Corresponding Authors

*E-mail: reza@mtu.edu.

*E-mail: anie@mtu.edu.

Author Contributions

Y.Y. carried out the TEM experiments and made the data analysis under the direction of R.S.Y., A.N., and R.F.K. R.S.Y. initiated the project and created the experimental protocols. G.M.O. performed DFT calculations. Y.Y., R.X., and J.L. performed the in situ XRD test and related data analysis. D.Z. carried coin cell CV testing under the direction of C.J. S.S. and D.D.M. supplied the samples. A.N., K.H., and H.A. helped to conduct the TEM analysis. Y.Y. and R.S.Y. wrote the manuscript and all the authors contributed to the discussion and revision of the manuscript.

Notes

The authors declare no competing financial interest.

■ ACKNOWLEDGMENTS

■ REFERENCES

(1) Truong, T. T.; Liu, Y.; Ren, Y.; Trahey, L.; Sun, Y. *ACS Nano* **2012**, *6*, 8067−8077.

(2) Boppana, V. B.; Jiao, F. *Chem. Commun. (Cambridge, U.K.)* **2011**, *47*, 8973−8975.

(3) Débart, A.; Paterson, A. J.; Bao, J.; Bruce, P. G. *Angew. Chem.* **2008**, *120*, 4597−4600.

(4) Chen, S.; Zhu, J.; Wu, X.; Han, Q.; Wang, X. *ACS Nano* **2010**, *4*, 2822−2810.

(5) Cheng, F.; Zhao, J.; Song, W.; Li, C.; Ma, H.; Chen, J.; Shen, P. *Inorg. Chem.* **2006**, *45*, 2038−2044.

(6) Wang, X.; Li, Y. *J. Am. Chem. Soc.* **2002**, *124*, 2880−2881.

(7) Chen, K.; Dong Noh, Y.; Li, K.; Komarneni, S.; Xue, D. *J. Phys. Chem. C* **2013**, *117*, 10770−10779.

(8) Devaraj, S.; Munichandraiah, N. *J. Phys. Chem. C* **2008**, *112*, 4406−4417.

(9) Li, L.; King, D. L. *Chem. Mater.* **2005**, *17*, 4335−4343.

(10) Li, L.; Nan, C.; Lu, J.; Peng, Q.; Li, Y. *Chem. Commun. (Cambridge, U.K.)* **2012**, *48*, 6945−6947.

(11) Yu, A.; Park, H. W.; Davies, A.; Higgins, D. C.; Chen, Z.; Xiao, X. *J. Phys. Chem. Lett.* **2011**, *2*, 1855−1860.

(12) Noailles, L. D.; Jhnson, C. S.; Vaughey, J. T.; Thackeray, M. M. *J. Power Sources* **1999**, *81*, 259−263.

(13) Johnson, C. S.; Thackeray, M. M. *J. Power Sources* **2001**, *97*, 437−442.

(14) Luo, J.; Zhang, J.; Xia, Y. *Chem. Mater.* **2006**, *18*, 5618−5623.

(15) Kijima, N.; Takahashi, Y.; Akimoto, J.; Awaka, J. *J. Solid State Chem.* **2005**, *178*, 2741−2750.

(16) Ohzuku, T.; Kitagawa, M.; Sawai, K.; Hiroi, T. *J. Electrochem. Soc.* **1991**, *138*, 360−365.

(17) Pang, W. K.; Peterson, V. K.; Sharma, N.; Zhang, C.; Guo, Z. *J. Phys. Chem. C* **2014**, *118*, 3976−3983.

(18) Rossouw, M. H.; Liles, D. C.; Thackeray, M. M. *Mater. Res. Bull.* **1992**, *27*, 221−230.

(19) Kumagai, N.; Sasaki, T.; Oshitari, S.; Komaba, S. *J. New Mater. Electrochem. Syst.* **2006**, *9*, 175−180.

(20) Johnson, C. S. *J. Power Sources* **2007**, *165*, 559−565.

(21) Huang, J.; Zhong, L.; Wang, C.; Sullivan, J. P.; Xu, W.; Zhang, L.; Mao, S. X.; Hudak, N. S.; Liu, X.; Subramanian, A.; Fan, H.; Qi, L.; K, A.; Li, J. *Science* **2010**, *330*, 1515−1520.

(22) Liu, X.; Wang, J.; Liu, Y.; Zheng, H.; Kushima, A.; Huang, S.; Zhu, T.; Mao, S. X.; Li, J.; Zhang, S.; Lu, W.; Tour, J. M.; Huang, J. *Carbon* **2012**, *50*, 3836−3844.

(23) McDowell, M. T.; Lee, S. W.; Harris, J. T.; Korgel, B. A.; Wang, C.; Nix, W. D.; Cui, Y. *Nano Lett.* **2013**, *13*, 758−764.

(24) Ghassemi, H.; Au, M.; Chen, N.; Heiden, P. A.; Yassar, R. S. *ACS Nano* **2011**, *5*, 7805−7811.

(25) Ghassemi, H.; Au, M.; Chen, N.; Heiden, P. A.; Yassar, R. S. *Appl. Phys. Lett.* **2011**, *99*, 1−3.

(26) Liang, W.; Yang, H.; Fan, F.; Liu, Y.; Liu, X. H.; Huang, J. Y.; Zhu, T.; Zhang, S. *ACS Nano* **2013**, *7*, 3427−3433.

(27) Wang, X.; Tang, D.; Li, H.; Yi, W.; Zhai, T.; Bando, Y.; Golberg, D. *Chem. Commun.* **2012**, *48*, 4812−4814.

(28) Su, Q.; Dong, Z.; Zhang, J.; Du, G.; Xu, B. *Nanotechnology* **2013**, *24*, 255705.

(29) Gao, Q.; Gu, M.; Nie, A.; Mashayek, F.; Wang, C.; Odegard, G. M.; Yassar, R. S. *Chem. Mater.* **2014**, *26*, 1660−1669.

(30) Nie, A.; Gan, L.; Cheng, Y.; Li, Q.; Yuan, Y.; Mashayek, F.; Wang, H.; Klie, R. F.; Schwingenschlogl, U.; Yassar, R. R. *Nano Lett.* **2015**, *15*, 610−615.

(31) Wang, F.; Yu, H. C.; Chen, M. H.; Wu, L.; Pereira, N.; Thornton, K.; Van der Ven, A.; Zhu, Y.; Amatucci, G. G.; Graetz, J. *Nat. Commun.* **2012**, *3*, 1201−1208.

(32) Zhu, Y.; Wang, J. W.; Liu, Y.; Liu, X.; Kushima, A.; Xu, Y.; Mao, S. X.; Li, J.; Wang, C.; Huang, J. Y. *Adv. Mater.* **2013**, *25*, 5461−5466.

(33) McDowell, M. T.; Woo Lee, S.; Wang, C.; Cui, Y. *Nano Energy* **2012**, *1*, 401−410.

(34) Liu, Y.; Liu, X. H.; Nguyen, B. M.; Yoo, J.; Sullivan, J. P.; Picraux, S. T.; Huang, J. Y.; Dayeh, S. A. *Nano Lett.* **2013**, *13*, 4876−4883.

(35) Liu, N.; Wu, H.; McDowell, M. T.; Yao, Y.; Wang, C.; Cui, Y. *Nano Lett.* **2012**, *12*, 3315−3321.

(36) Wu, M.; Lee, J. Y.; Lin, J. C. *J. Phys. Chem. B* **2005**, *109*, 23279−23284.

(37) Desilvestro, J.; Haas, O. *J. Electrochem. Soc.* **1990**, *137*, 17−21.

(38) Santhanagopalan, S.; Balram, A.; Meng, D. D. *ACS Nano* **2013**, *7*, 2114−2125.

(39) Portehault, D.; Cassaignon, S.; Baudrin, E.; Jolivet, J. P. *Chem. Mater.* **2007**, *19*, 5410−5417.

(40) Kumar, V. G.; Gnanaraj, J. S.; Salitra, G.; Abramov, A.; Gedanken, A.; Aurbach, D.; Soupart, J. B.; Rousche, J. C. *J. Solid State Electrochem.* **2004**, *8*, 957−967.

(41) Post, J. E.; Von Dreele, R. B.; Buseck, P. R. *Acta Crystallogr.* **1982**, *38*, 1056−1065.

(42) Lan, B.; Yu, L.; Lin, T.; Cheng, G.; Sun, M.; Ye, F.; Sun, Q.; He, J. *ACS Appl. Mater. Interfaces* **2013**, *5*, 7458−7464.

(43) Galindo, H. M.; Carvajal, Y.; Njagi, E.; Ristau, R. A.; Suib, S. L. *Langmuir* **2010**, *26*, 13677−13683.

(44) Liu, X. H.; Zhang, L. Q.; Zhong, L.; Liu, Y.; Zheng, H.; Wang, J. W.; Cho, J. H.; Dayeh, S. A.; Picraux, S. T.; Sullivan, J. P.; Mao, S. X.; Ye, Z. Z.; Huang, J. Y. *Nano Lett.* **2011**, *11*, 2251−2258.

(45) Ling, C.; Mizuno, F. *Chem. Mater.* **2012**, *24*, 3943−3951.

(46) Johnson, C. S.; Dees, D. W.; Mansuetto, M. F.; Thackeray, M. M.; Vissers, D. R.; Argyriou, D.; Loong, C. K.; Christensen, L. *J. Power Sources* **1997**, *68*, 570−577.

(47) Balaya, P.; Li, H.; Kienle, L.; Maier, J. *Adv. Funct. Mater.* **2003**, *13*, 621−625.

(48) Poizot, P.; Laruelle, S.; Grugeon, S.; Dupont, L.; Tarascon, J. M. *Nature* **2000**, *407*, 496−499.

(49) Chen, C.; Ding, N.; Wang, L.; Yu, Y.; Lieberwirth, I. *J. Power Sources* **2009**, *189*, 552−556.

(50) Riedl, T.; Gemming, T.; Wetzig, K. *Ultramicroscopy* **2006**, *106*, 284−291.

(51) Wang, Z. L.; Yin, J. S.; Jiang, Y. D.; Zhang, J. *Appl. Phys. Lett.* **1997**, *70*, 3362−3364.

(52) Kurata, H.; Colliex, C. *Phys. Rev. B* **1993**, *48*, 2102−2108.

(53) Schmid, H. K.; Mader, W. *Micron* **2006**, *37*, 426−432.

(54) Zhang, S.; Livi, K. J. T.; Gaillot, A. C.; Stone, A. T.; Veblen, D. R. *Am. Mineral.* **2010**, *95*, 1741−1746.

(55) Jahn, H. A.; Teller, E. *Proc. R. Soc. London, Sect. A: Math. Phys. Sci.* **1937**, 220−235.

(56) Cramer, C. J.; Truhlar, D. G. *Phys. Chem. Chem. Phys.* **2009**, *11*, 10757−816.

(57) Vasconcelos, P. M.; Wenk, H. R.; Echer, C. *Am. Mineral.* **1994**, *79*, 80−90.

(58) Yang, Z.; Trahey, L.; Ren, Y.; Chan, M. K. Y.; Lin, C.; Okasinski, J.; Thackeray, M. M. *J. Mater. Chem. A* **2015**, *3*, 7389−7398.